LAWRENCE
LIVERMORE
NATIONAL
LABORATORY

UCRL-CONF-206988

Buoyancy-Driven Polymerase Chain Reaction (PCR) Devices

K. D. Ness, E. K. Wheeler, W. Benett, P. Stratton, A. Christian, A. Chen, J. Ortega, T. H. Weisgrabber, K. E. Goodson

October 1, 2004

Transport Phenomena in Micro and Nano Devices
Kona Coast, HI, United States
October 17, 2004 through October 21, 2004

Disclaimer

Buoyancy-Driven Polymerase Chain Reaction (PCR) Devices

Kevin D. Ness

Lawrence Livermore National Laboratory, Livermore, California 94550, and

Department of Mechanical Engineering, Stanford University, Stanford, California 94305

Elizabeth K. Wheeler, William Benett, Paul Stratton, Allen Christian, Alice Chen, and

Todd H. Weisgraber

Lawrence Livermore National Laboratory, Livermore, California 94550

Kenneth E. Goodson

Department of Mechanical Engineering, Stanford University, Stanford, California 94305

Polymerase chain reaction (PCR) facilitates DNA detection by significantly increasing the concentration of specific DNA segments. A new class of PCR instruments uses a buoyancy-driven re-circulating flow to thermally cycle the DNA sample and benefits from reduced cycle times, low sample volumes, a miniaturized format, and low power consumption. This paper analyzes a specific buoyancy PCR device in a micro-channel 'race-track' geometry to determine key parameters about PCR cycle times and other figures of merit as functions of device dimensions. The 1-D model balances the buoyancy driving force with frictional losses. A hydrostatic pressure imbalance concept is used between the left and right sides of the fluid loop to calculate the buoyancy driving force. Velocity and temperature distributions within the channels are determined from two-dimensional analysis of the channel section, with developing region effects included empirically through scaled values of the local Nusselt number. Good agreement between

four independent verification steps validate the 1-D simulation approach: (1) analytical expressions for the thermal entrance length are compared against, (2) comparison with a full 3-D finite element simulation, (3) comparison with an experimental flowfield characterization, and (4) calculation of the minimum PCR runtime required to get a positive PCR signal from the buoyancy-driven PCR device. The 1-D approach closely models an actual buoyancy-driven PCR device and can further be used as a rapid design tool to simulate buoyancy PCR flows and perform detailed design optimizations studies.

INTRODUCTION

Direct detection of specific DNA targets is difficult because of small nanometer size molecules and low sample concentrations. Nucleic acid based detection schemes greatly benefit from the ability to amplify over a billion fold specific DNA segments using a technique known as polymerase chain reaction (PCR).[1] Most PCR devices achieve this amplification by thermally cycling a fluid between a high DNA denaturing temperature (~94 ^{o}C) and a low DNA annealing temperature (~57 ^{o}C) with an optional ~72 ^{o}C hold for DNA extension. Since the DNA amplification reaction is thermally regulated, PCR devices must uniformly, precisely and reproducibly control the fluid temperature to obtain quantitative, reliable DNA measurements. Microfabrication is well suited for developing a temperature control system for DNA amplification because of the large surface-to-volume ratios in microscale devices, as well as the possibility of integrating temperature sensors and heaters. Increased surface area and reduced volumes allow for

faster and more uniform temperature cycling in microfabricated PCR devices.[2] Microfabricated PCR devices also benefit from reduced reagent consumption and an easier integration with front-end sample preparation techniques, which typically produce small volumes of sample (~10-100 μL).[3]

This paper focuses on a novel approach to perform the thermal cycling for PCR, which uses buoyancy forces to cycle the fluid between heating and cooling zones. This is different from the typical PCR thermal cycling approaches, which generally heat and cool the package containing the PCR fluid mixture.[4] Multiple zones at different temperatures generate fluid density gradients, which induce a stable buoyancy-driven re-circulating flow under certain conditions. The circulating flow-field is used as the transport mechanism to thermally cycle the DNA sample between the required PCR temperatures (~57^{o}C-~94^{o}C). Buoyancy driven PCR, natural convection PCR, or convective PCR (CPCR) has previously been demonstrated using three different architectures. Krishnan *et al.* used a Rayleigh-Benard convection cell (with a heated bottom and cooled top) to amplify a 295-bp human DNA template sample in approximately 90 minutes,[5] Wheeler *et al.* used a micro 'race-track' configuration loop to amplify a 58-bp and 160-bp *Erwinia herbicola* sample in approximately 20 minutes,[6 7 8] and Braun *et al.* used a cylinder (1 x 5 mm) with an infrared laser focused along the cylinder axis to amplify a 96-bp piece of λ-DNA.[9] The 'race-track' loop structure gives the user more control over the thermal history and cycle time, thus, is the architecture of choice for the present study.

Using buoyancy-driven PCR to achieve the required thermal cycling is a logical step in the evolution of PCR instrumentation. Since temperature differences (or cycling) are inherently required to drive the biological reaction or amplification process forward, natural convective effects can be generated and exploited, thus positive energy or work extracted directly from the assays biological thermal requirements.

An example buoyancy driven PCR device is shown in Fig. 1. There are two main temperature control regions (a left side and a right side) containing multiple resistive heater segments, temperature sensors and heat spreaders. The top part of the device incorporates a copper block as a passive heat sink to lower the fluid temperature by removing heat to the ambient. An optical window at the loop bottom allows for real-time monitoring of fluorescent species produced during the amplification process (RT-PCR). The fluidic chamber or channel is sandwiched between two circuit board plates surrounded by an insulating package. The outer packaging reduces the power consumption of the device by insulating the heated elements from the environment. However, the package is not a perfect insulator and does heat up during operation so any model must account for heat loss through the package and out to the environment by free convection.

This paper develops and compares with experimental data a new, simple model for heat and fluid flow in buoyancy-driven PCR devices. The model yields key information about PCR cycle times and other figures of merit as functions of device dimensions. The solution method simplifies the governing equations to an approximate one-dimensional

form and uses a buoyancy-developed hydrostatic pressure imbalance concept to drive the flow, which is counter-balanced by viscous forces. An emphasis is placed on the fluid temperature distribution about a vertical symmetry plane (left/right side of the device) to calculate this buoyancy induced hydrostatic pressure imbalance. The velocity and temperature distributions within the channels are determined from two-dimensional analysis of the channel section, with developing region effects included empirically through scaled values of the local Nusselt number.[10] The modeling is validated using experimental data from a device fabricated using modified circuit board patterning technologies. Four independent validation steps are performed to check the 1-D simulation approach: (1) analytical expressions for the thermal entrance length are compared against, (2) comparison with a full 3-D simulation, (3) comparison with an experimental flow field characterization, and (4) calculation of a minimum PCR runtime to get a positive PCR signal from the buoyancy-driven PCR device.

THERMAL AND FLUIDIC MODELING

Experimental and theoretical investigation of single-phase natural convection in enclosed structures dates back to the early 1940's.[11] In addition, there has been much work on natural convection loops or thermosyphons. [12] [13] Many excellent reviews of this field exist and can be found in the following references.[14] [15] [16] [17] This earlier work focused primarily on *macro-scale* devices (~centimeters), [18] generally including phase change,

and not the specific geometries relevant for use with biological assays and/or simple micro-fabrication compatible strategies. The present work develops a comprehensive modeling approach and guidelines for the implementation of *micro-scale* natural convection loops as PCR thermal cyclers.

1D Simplified Model

This work leverages the simple geometry of the loop to develop a simplified 1-D modeling approach for buouyancy-driven PCR devices. The calculation approach yields predictions that are consistent with more detailed simulations and with experimental data. The 1-D approach is computationally efficient and gives insight into the buoyancy driving mechanism. The solution approach proposed here for PCR iteratively solves a 1-D thermal energy equation and a 1-D momentum equation. Variations in the spanwise channel direction are neglected by area averaging the governing equations across the channel cross-section. The loop structure is uncurled and treated as a straight channel with periodic end boundary conditions. The body force term is proportional to the local dot product of the gravity vector and the streamwise coordinate. To account for the variety of devices analyzed, both in terms of geometries and thermal boundary conditions, the conservation equations are discretized and solved iteratively based on a control volume formulation.[19]

The modeling is subject to the Boussinesq approximation and assumes constant fluid properties, steady state conditions, fluid is hydrodynamically fully developed, thermally developing regions are accounted for when appropriate, conjugate heat transfer and axial wall conduction are neglected (however, wall radial conduction is included). Corner effects are neglected for the fluid flow problem and in determining the local heat transfer coefficient, which places an upper bound on the calculated average velocity. The three area-averaged governing equations are written in 1-D along the direction of fluid motion. These include mass conservation for incompressible flow

$$A_c V_{ave} = Q\,, \tag{1}$$

conservation of momentum (also integrated along the entire channel length) with the first and second terms representing the viscous frictional loses and the buoyancy driving force, respectively,

$$A_p\, f\rho V_{ave}^2 \big/ 2 + \int \rho_o \beta g (T_o - T_m) dV = 0\,, \tag{2}$$

and conservation of thermal energy

$$\frac{d}{dx}\left(\rho V_{ave} c_p T_m\right) + \frac{d}{dx}\left(-k\frac{d}{dx}T_m\right) = \frac{\left(h_{Nu}(T_w - T_m)\left(A_p\right) + h_{NC}(T_\infty - T_m)\left(A_p\right)\right)}{\left(dx_{CV}\cdot w\cdot d\right)}\,. \tag{3}$$

Here, A_c is the cross-sectional area, V_{ave} is the area-averaged velocity, Q is the bulk flow rate, A_p is the wetted perimeter, f is the Moody friction factor for hydrodynamically fully developed flow trough rectangular channels,[10] ρ is the fluid density (ρ_o is the reference density at a reference temperature, 'T_o', defined as the average temperature between the denaturing temperature and the annealing temperature), β is the coefficient of thermal expansion (evaluated at T_o), g is gravity, c_p is the specific heat, T_m is the mixed-mean fluid temperature, V is the fluid volume, k is the fluid thermal conductivity, h_{Nu} is the convection coefficient as defined by the thermally developing, hydrodynamically fully developed Nusselt relations for constant surface temperatures,[10] T_w is the wall fluid temperature, h_{NC} is a modified convection coefficient including radial wall conduction resistances, a natural convection convection coefficient, and thermally developing, hydrodynamically fully developed Nusselt relations for constant heat flux,[10] T_∞ is the ambient temperature, dx_{CV} is the discretized control volume slice length along the channel length, w is the channel width, and d is the channel depth. Only one convection coefficient, 'h_{Nu}' or 'h_{NC}', is used for a single control volume depending on the local applied boundary condition, either constant temperature or heat lost to the environment.

Solution Algorithm

This algorithm begins with an initial guess for the cross-sectional area averaged velocity based on scaling arguments (see the Results and Discussion section) to solve the thermal energy equation for the axial mixed mean fluid temperature. A Gauss-Seidel iteration

scheme is used to numerically solve the thermal energy equation until the temperature distribution converges within an acceptable error using global energy conservation as the convergence test.

Once the temperature distribution is known the buoyancy force is calculated as

$$\int \rho_o \beta g (T_o - T_m) dV = A_c \left[- \int_0^{L_T/2} \rho_o \beta g(s)(T_o - T_m) ds + \int_{L_{Tt}/2}^{L_T} \rho_o \beta g(s)(T_o - T_m) ds \right], \qquad (4)$$

$$\text{"left column of fluid"} \qquad\qquad \text{"right column of fluid"}$$

which is based on the left/right fluid column weight difference. Here, *s* is the streamwise coordinate along the closed loop device and L_T is the total centerline loop length. The buoyancy driving force (4), which is balanced by the viscous frictional force, is related through the cross-sectional area to a net buoyancy pressure difference. A thermally induced buoyancy pressure gradient is calculated from the buoyancy pressure difference and substituted into the streamwise momentum equation to solve for the velocity profile

$$\frac{dp}{ds} = \frac{\Delta p}{\Delta s} = \frac{\Delta W / A_c}{L_T} \leftarrow \frac{\text{"}buoyancy\ \ pressure\ difference\text{"}}{\text{"}total\ channel\ length\text{"}}. \qquad (5)$$

Here, *p* is the pressure and ΔW is the weight difference between the left/right fluid columns.

The viscous, fully-developed momentum equation for the velocity profile with an applied pressure gradient for rectangular geometries has been determined previously.[20] Using this analytical series expansion expression and the derived streamwise buoyancy pressure gradient a new average velocity is calculated ($dp/ds = dp/dx$).

$$u = -\frac{16a^2}{\mu\pi^3}\left(\frac{dp}{dx}\right)\sum_{i=1,3,\ldots}^{\infty} -1^{(i-1)/2}\left[1-\frac{\cosh\left(i\pi z/2a\right)}{\cosh\left(i\pi b/2a\right)}\right]\cdot\frac{\cos\left(i\pi y/2a\right)}{i^3}. \qquad (6)$$

Here, a is half the width, b is half the depth, and μ is the dynamic viscosity.

In summary, the solution algorithm obtains the temperature distribution from an initial average velocity estimate, relates this to a fluidic driving force, balances this with a frictional force to obtain a new average velocity and iterates until the change in average velocity is below 0.1%.

Thermal Entrance Length

When the wall thermal boundary conditions change, the fluid is disturbed from a fully-developed temperature profile and the heat transfer coefficients are modified as well. This is analogous to the entrance of a fluid into a pipe; specifically the thermal entrance

length over which the fully-developed profile is established. The convection coefficients are modified in the entrance regions empirically through scaled values of the local Nusselt number.[10] Simple analytical expressions for the thermal entrance length can be expressed based on the time required for heat to diffuse half the channel depth,

$$L_e = \left(\frac{d}{2}\right)^2 \frac{V_{\max}}{\alpha}. \qquad (7)$$

Here, L_e is the thermal entrance length, V_{max} is the maximum fluid velocity, and α is the thermal diffusivity. For the devices analyzed in this study thermal entrance lengths are approximately 1-10 mm in length and mainly depend on the channel hydraulic diameter. The numerical simulation qualitatively captures the correct trend in thermal entrance length with channel depth for a given CPCR geometry when compared with this analytical expression.

3-Dimensionsal Finite Element Calculation

The incompressible flow package of ALE3D (internal to LLNL) is used to simulate the flow in the PCR channel.[21] Two computational grids are used in this study. Grid 1 has a total 12,480 elements, grid 2 has a total of 18,432 elements, grid 1 has 5 elements in the *z*-direction (depth), grid 2 has 4 elements in the z-direction (depth), grid 2 has more

elements in the streamwise flow direction than grid 1. Both of these grids are graded near the walls at each value of *z*, allowing resolution of the boundary layer-like velocity profiles that are anticipated to occur near the walls. The fluid boundary conditions are no-slip/no-penetration along the entire channel. The temperature boundary conditions on the straight portions of the channel are T_{hot} = 367K (left side) and T_{cold} = 330K (right side). The other channel surfaces are adiabatic for one simulation. The working fluid is taken to be water, where the physical properties are evaluated at (T_{hot} + T_{cold}) /2.0 to give $\beta = 615.6\times10^{-6}$ K^{-1}, $\mu = 3.715\times10^{-4}$ m^2/s, $\rho = 974.6$ kg/m^3, k = 0.668 W/m·K, and c_p = 4193.8 J/kg·K, where β is the coefficient of thermal expansion, μ is the dynamic viscosity, ρ is the fluid density, k is the thermal conductivity, and c_p is the specific heat at constant pressure. Throughout the simulations, these properties are taken to be constant. However, these properties do exhibit changes with changing temperature. In fact, from T_{hot} to T_{cold}, the relative change of β is on the order of 30% and that of μ on the order of 70%. In future simulations, the temperature dependence of these properties should be taken into consideration.

At time t = 0, the fluid velocity is initialized to zero over the entire channel and the temperature boundary conditions are turned on. For these initial computations, an explicit, first-order accurate time integration scheme is used to capture the transient behavior of the flow. Both simulations are run until t $\approx$ 90 seconds, at which time the velocity magnitude is changing less than 0.005%.

RESULTS AND DISCUSSION

Comparison of 1-D Model with 3-D Simulation Results and Digital Particle Image Velocimetry Data

The model developed here has been briefly discussed in a previous publication (Wheeler *et al*.[8]), which showed reasonable agreement between the 1-D predictions and the 3-D simulations and digital particle imaging velocimetry (DPIV). For clarity and the benefit of the reader, we reproduce the essential figures from that previous work as Figure 2 in this publication. Figure 2a shows a comparison of the streamwise vertical velocity for the 1-D and 3-D simulations. The 1-D simulation predicts a larger magnitude velocity compared to the 3-D simulation and is attributed to the increased fluidic resistance not captured by the 1-D approach in modeling flow around corners (1-D model simulates a straight channel with periodic end boundary conditions). The flow is 'plug-like' in the width direction and parabolic in the depth direction as expected based on the channel aspect ratio of ~10 in this simulation. Figure 2b compares the 3-D simulation with an experimental technique (DPIV), which measures the velocity field, to validate the 3-D simulation. Very good agreement is seen over a portion of the channel width. DPIV data is only obtained over the bottom portion of the channel based on experimental limitations. Additional details about the DPIV experiment are discussed in Wheeler *et al.*[8] Figure 2 is included here to demonstrate the 1-D approach closely models an actual

buoyancy-driven PCR device and can be used as a rapid design tool to simulate these flows in just minutes on a standard PC.

Calculation of the Minimum Required PCR Runtime

Figure 3 plots the energy consumed during PCR operation versus thermal cycling time for different concentrations of a 160-bp segment of genomic DNA from *Erwinia herbicola* (Eh). Sequential experimental runs reduced concentration and time until a positive PCR signal could not be visualized using a stained gel-electrophoretic assay. A minimum run time was observed for a positive PCR signal between 4-9 minutes (including a 11-minute slow ramp start up time based on electronic issues). A separate experiment on a standard MJ Research PTC-200 thermal cycler determined at least 20 thermal cycles are required to visualize a positive PCR signal with the stained gel-electrophoretic assay. The simulation predicts for 20 thermal cycles a run time of 8.5 minutes, which falls within the experimentally determined 4-9 minute range.

Temperature and Velocity Profiles (1-D Simulation)

The main geometric factor governing the thermal and velocity profile is the hydraulic diameter of the fluidic channel, mainly the channel depth because of typically large

aspect ratios. The critical depth dimension is constrained between an upper and lower limit from the requirements of the biological reaction and overall device performance, respectively. A requirement of a few minutes per cycle for device operation sets the lower limit channel depth; the smaller the depth dimension the larger the fluidic resistance and the lower the flow rate. The upper limit on the depth dimension is based on the condition that the fluid reach the required PCR temperatures. To ensure this, the flow rate cannot be so large the thermal entrance length is greater than the length of the heating/cooling sections. From these two requirements and the chosen footprint (overall height 25.1 mm, channel width 3.6 mm, inner loop radius 1.8 mm) the depth lower and upper limits are 100 and 800 μm.

The mixed-mean temperature distribution along the channel is plotted in Fig. 4a versus channel length for different channel depths. The channel is broken into 4 different zones. Each zone has a different thermal boundary condition; zone 1 has a constant wall temperature (94 ^{o}C), zone 2 and 4 loose heat to the ambient and use constant heat flux boundary conditions, zone 3 has a constant wall temperature (57 ^{o}C). As can be seen in zone 1 and 3, the thermal entrance length increases as the depth increases. This is easily understood when the velocity profile along the depth direction is plotted as a function of channel depth (Fig. 4b). As channel depth increases the velocity also increases. The residence time a fluid packet spends in the heating/cooling section decreases and thus the thermal entrance length should increase. Reasons for the setting the lower depth limit at 100 μm are seen in Fig 4b because as the average velocity drops below ~0.3 mm/sec the cycle time becomes larger than the few minute cycle time requirement.

One interesting feature from the simulation velocity plot (Fig. 4b) is the fact the peak velocity at the centerline of the channel is governed solely by the channel depth even though the channel is rectangular in nature. The peak velocity is marked for each channel depth with a diamond by searching the velocity profile across the cross-section for the maximum value. The maximum always occurs at the center of the channel. A dashed line plots the maximum velocity versus channel depth using the calculated pressure gradient and an analytical expression for viscous fully developed flow between two flat plates.[20] The red diamonds and the analytical dashed line fall directly on top of each other indicating the channel depth dominates the fluidic resistance thus controlling the flow rate (for these aspect ratios ~ 4-36).

To understand the buoyancy driving force, which balances the viscous frictional force, it is helpful to plot the individual buoyant force components used in this analysis versus the channel depth. Each bar pair (a low and a high value) in Fig. 4c corresponds to a particular channel depth. Each individual bar is a measure of the hydrostatic pressure (at the loop bottom) or the weight of fluid (divided by the cross-sectional area) for the left and right fluid columns of the loop. The left column of fluid is at a higher temperature and lower density compared to the right column of fluid based on the heating configuration. The buoyant driving force is related to the net difference in hydrostatic pressure between the left and right columns of fluid. The hydrostatic pressure imbalance can be extracted from the red dotted line between the left (hot) and right (cold) bar pairs. The net difference between the left/right column hydrostatic pressure decreases as the

channel depth increases. This decline in driving force is understood based on a reduction in the fluidic resistance causing an increase in flow rate, which increases the thermal entrance length. It is the growing thermal entrance length with increasing channel depth that causes the buoyant driving force to drop. A larger thermal entrance length means cooler fluid penetrates into the left heater region (zone 1) and hotter fluid penetrates into the right cooling region (zone 3). This approaches a thermal profile with hot fluid on top and cold fluid on the bottom, in addition, to a left/right thermal symmetry about the vertical; therefore, the buoyancy force should decrease. An exact left/right thermal symmetry is not obtained for the cases analyzed here (channel depth up to 800 μm) so the buoyant driving force does not reduce to zero.

Another way to view the buoyant driving force is to look at the buoyant pressure gradient used to generate motion in Fig. 4d. The difference in hydrostatic pressure between the left and right columns of fluid is equated to a pressure drop and then a pressure gradient ($dp/dx = \Delta p/L_T$). The pressure gradient is seen to decrease with increasing channel depth even though the average velocity increases with channel depth. This is attributed to the fluidic resistance decreasing faster than the decreasing driving force as channel depth is increased. The 100-micron channel depth bar pairs (Fig. 4c) can now be understood by looking at the thermal profile. Three observations, the thermal entrance length is very small, zones 2 and 4 significantly alter the thermal profile (reduce the temperature thus increase the density), and the left/right temperature anti-symmetry at a maximum, account for the large magnitude of each bar (for d=100 μm) in Fig 4c when compared to the 200 micron case and the largest driving force (or pressure gradient) in Fig. 4d.

Scaling Analysis for Fluid Velocity and Cycle Time

A scaling analysis is performed to rapidly determine the average velocity of fluid in a closed loop rectangular channel for use in buoyancy PCR devices. This analysis balances buoyant work with kinetic energy and frictional work losses. Internal fluid is at two different discrete temperatures, with all the fluid between two heaters (both of length, L_{heater}) to the left of the vertical center at T_{hot} and the fluid to the right of the vertical center at T_{cold} ($\Delta T = T_{hot} - T_{cold}$). The temperature profile generates a buoyancy force, which acts to accelerate the fluid around the channel loop. The buoyancy forces can be related to the difference in weight between the left (hot) and right (cold) potions of the fluid ($B = \Delta mg$). With the fluid initially at rest ($t = 0$), a balance exists between the product of the buoyancy force and the total distance the plug of fluid has traveled to the sum of the kinetic energy for this fluid plug and the wall friction times the total distanced traveled. This is shown in the following expression with the characteristic length equal to the total distance traveled

$$\underset{\text{"weight difference"}}{\Delta mgL} = \underset{\text{"kinetic"}}{\frac{1}{2}mV_{ave}^2} + \underset{\text{"frictional losses"}}{F_{Friction}L} \quad ; \quad \underset{\text{"characteristic length"}}{L = V_{ave}t} . \tag{8}$$

Assuming the aspect ratio of the channel is greater than ~5, the local wall shear stress for flow between parallel flat plates can be used ($\tau = 6\mu V_{ave}/d$; $F_{Friction} = \tau A_p$).[20] An expression for the average velocity as a function of time is given below for a fluid plug moving around a rectangular channel

$$V_{ave}(t) = \frac{\underset{\text{"buoyancy"}}{A_c L_{heater} \rho_o \beta \Delta T g\, t}}{\underset{\text{"inertial"}}{\frac{1}{2}\rho V} + \underset{\text{"friction"}}{\frac{6\mu A_p}{d} t}}. \qquad (9)$$

Figure 5 shows the average fluid velocity reaches a steady state value of ~2.4 mm/s in ~1 second for a 75 micro-litter plug of fluid in a closed loop rectangular channel (400 μm x 3.6 millimeters) of height around 2.5 centimeters tall. The average cycle time can easily be calculated by dividing the total loop path length by the average fluid velocity.

CONCLUDING REMARKS

This work highlights benefits of buoyancy-driven PCR, including precision temperature regulation, fast thermal cycling, low power consumption, a miniaturized format and compatible with a disposable plastic sample bag. Precise temperature regulation comes from the very small channel depth (~500 μm) and heating on both or all sides. This small

distance ensures a flat thermal profile ($T_{wall} \cong T_m$) once thermally fully developed conditions are reached. Fast thermal cycling (~5-40 seconds calculated; ~25 seconds experimentally determined) comes from the moderate average velocities (~2 mm/sec) and small loop distances (~50 mm). Low power consumption comes from the need to only heat the device up once.[8] Power requirements are important for future portable handheld PCR instruments. Thermal cycling of the container, as required in typical PCR instrumentation, is not needed in the device presented in this paper. If the exterior packaging is properly insulated the power consumption should approach the theoretical minimum for power consumption (heating only the thermal mass of a portion of the fluid sample itself and doing this only once) in the buoyancy driven format. Since, the sample is placed in a plastic bag and sandwiched between two cards the device is easily scalable in this miniaturized format. The plastic bag insert is used to convert the device to a disposable format.

The main drawback from using the buoyancy driven approach in a 'race-track' configuration is the cross-sectional velocity variation. Velocity gradients in the span-wise direction cause the genomic DNA or amplicons at different spatial locations in the cross-section (or varying distances from the wall) to have different cycle times. The implication of this dispersion in cycle time is a loss of thermal time history control. For example, an amplicon near the wall advected with the flow has a small local velocity while an amplicon near the geometric center of the channel is traveling at the maximum velocity. However, the variation in cycle time because of span-wise velocity gradients is tightened by molecular diffusion. PCR usually requires between 20-35 cycles before the

concentration of amplicon or probe is large enough to produce a detectible positive signal above the noise floor. Based on this many loop cycle requirement for detectable PCR amplification, certain restrictions on the diffusive Peclet number are usually met and the concentration-tracking problem can be viewed as one of Taylor dispersion. When these conditions are met the bulk velocity can be used as a good measure to determine the CPCR instruments cycle time.

ACKNOWLEDGEMENTS

This work was funded by the Engineering Exploratory Research and Development funds from the Laboratory Directed Research and Development program at Lawrence Livermore National Laboratory. Funding from this program is gratefully acknowledged. K.D.N. would like to thank Lara Daily, David Clague, Ankur Jain and Bill King for many useful discussions about the 1-D modeling approach. This work was performed under the auspices of the U.S. Department of Energy by University of California, Lawrence Livermore National Laboratory under Contract W-7405-Eng-48.

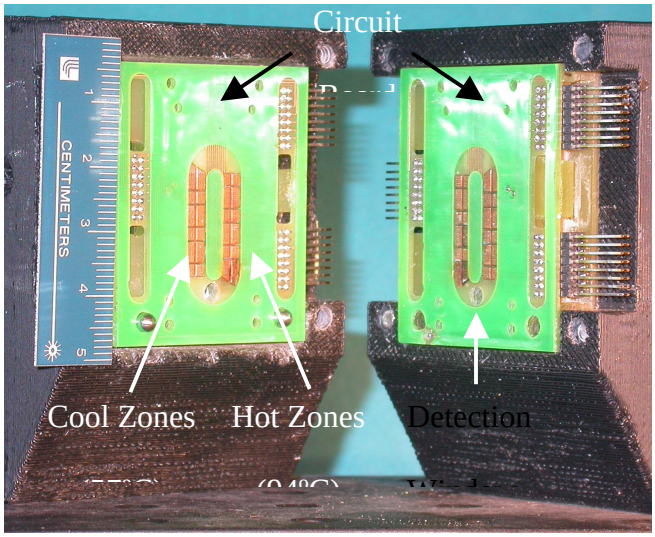

Figure 1.

Author: Kevin D. Ness

FIG. 1. A picture of LLNL's microfabricated device using two circuit board materials containing a grooved surface and a plastic bag (not shown) are sandwiched together to perform buoyancy-driven PCR. Each vertical, straight section can independently maintain a constant temperature and there is an optical detection window in the curved bottom section.

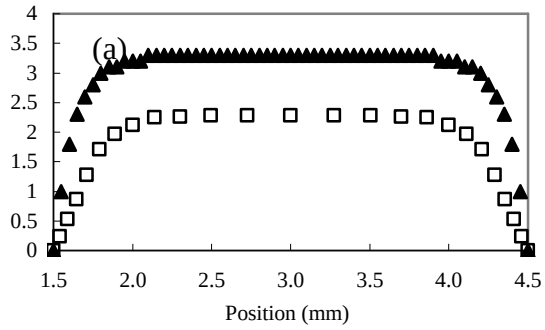

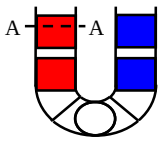

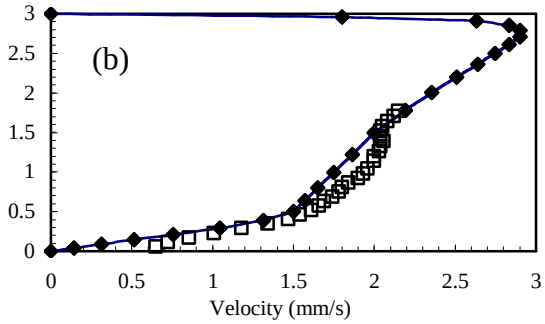

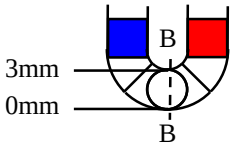

Fig. 2

Author: Kevin D. Ness

FIG. 2. Streamwise velocity components versus channel width (at half the channel depth) along the dashed lines shown in the drawing inserts. (a) Vertical velocity profile across the channel width for the 1-D simulation (closed triangles) and the 3-D simulation (open squares). (b) Horizontal velocity components across the channel width in the bottom curved section for the 3-D simulation (closed diamonds) and from DPIV (open squares).

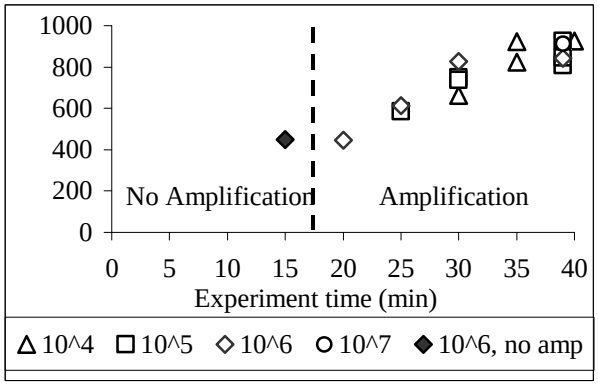

Fig. 3

Author: Kevin D. Ness

FIG. 3 Experimental determination of the minimum run time using a buoyancy-driven PCR thermal cycler to get a successful PCR amplification. A 160-bp segment from genomic *Erwinia herbicola* DNA (10^4–10^7 /mL) is amplified and detected using a gel-electrophoretic assay. A 4-9 minute window is determined as the minimum run time to obtain a successful amplification (all PCR runs require an 11 minute start-up time).

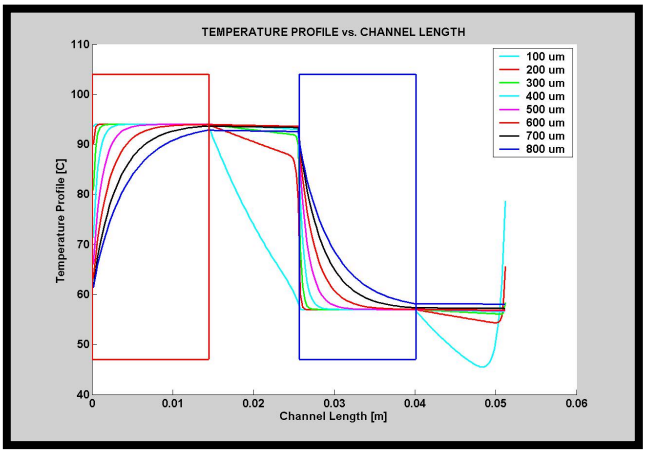
TEMPERATURE PROFILE vs. CHANNEL LENGTH
Temperature Profile [C]
Channel Length [m]
100 um
200 um
300 um
400 um
500 um
600 um
700 um
800 um

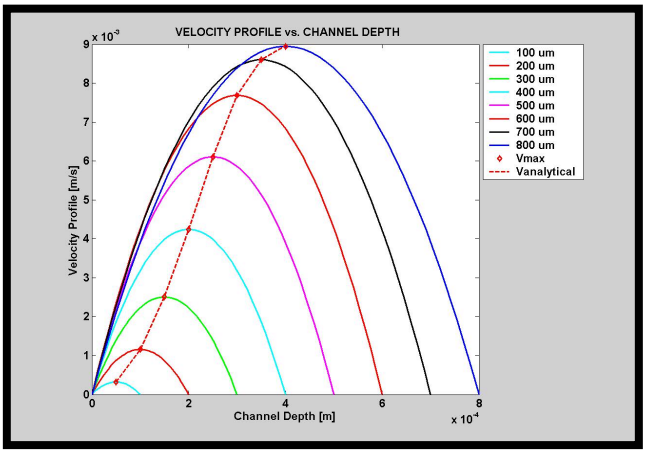
VELOCITY PROFILE vs. CHANNEL DEPTH
x 10^-3
Velocity Profile [m/s]
Channel Depth [m]
x 10^-4
100 um
200 um
300 um
400 um
500 um
600 um
700 um
800 um
Vmax
Vanalytical

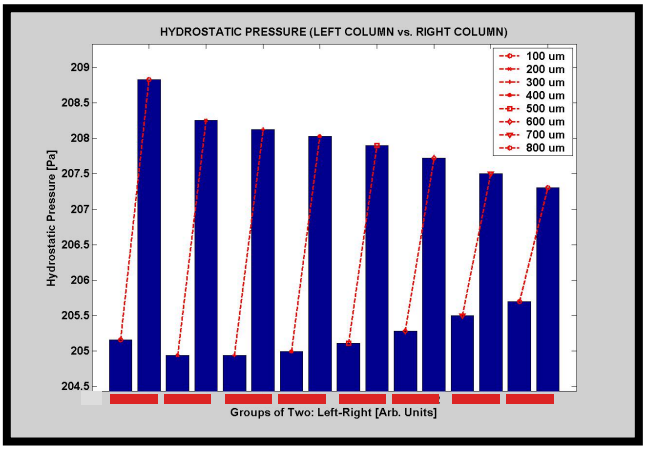
HYDROSTATIC PRESSURE (LEFT COLUMN vs. RIGHT COLUMN)
Hydrostatic Pressure [Pa]
Groups of Two: Left-Right [Arb. Units]
100 um
200 um
300 um
400 um
500 um
600 um
700 um
800 um

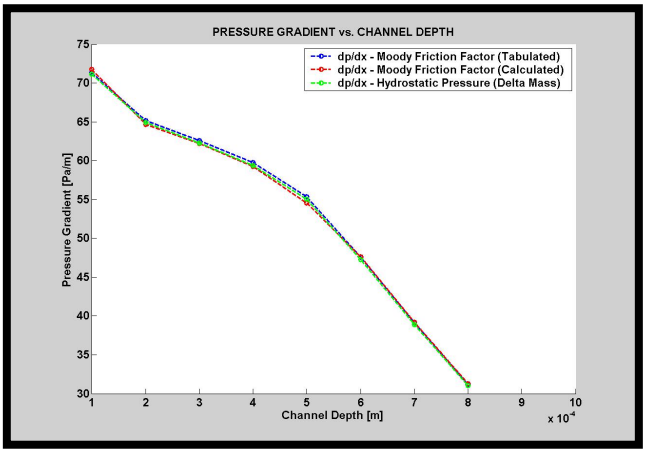
PRESSURE GRADIENT vs. CHANNEL DEPTH
Pressure Gradient [Pa/m]
Channel Depth [m]
x 10^-4
dp/dx - Moody Friction Factor (Tabulated)
dp/dx - Moody Friction Factor (Calculated)
dp/dx - Hydrostatic Pressure (Delta Mass)

Fig. 4

Author: Kevin D. Ness

FIG. 4 Typical results from the 1-D modeling approach for a buoyancy-driven PCR device (loop height 25.1 mm, channel width 3.6 mm, inner loop radius 1.8 mm, depth 100-800 microns). (a) Mixed mean temperature distribution along the channel axis for different channel depths. (b) Parabolic velocity profile for different channel depths. Diamonds indicate location of maximum velocity and the dashed line uses an analytic expression for viscous fully developed flow between two flat plates. (c) Bar pairs (small and large) represent hydrostatic pressure at the loop bottom for the left and right columns of fluid, respectively. (d) Equivalent pressure gradient to drive flow at an average velocity through a straight rectangular tube of length equal to the axial loop length that matches the average fluid velocity obtained by balancing the buoyant driving force and viscous friction.

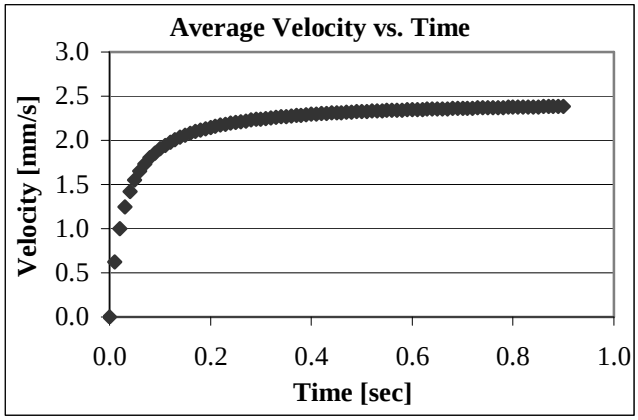

Fig. 5

Author: Kevin D. Ness

FIG. 5 Scaling analysis for average velocity in buoyancy-driven PCR devices. Balancing the buoyant driving force between kinetic energy and wall frictional losses quickly estimate the average fluid velocity. The buoyancy force is obtained from an assumed

temperature distribution with all fluid under the left heater at T_{hot} and all fluid under the right heater at T_{cold}.

REFERENCES

[1] K. B. Mullis, F. Faloona, S. Scharf, R. Saiki, G. Horn, and H. Elrich, “Specific enzymatic amplification of DNA invitro - the polymerase chain-reaction,” Cold Spring Harbor Symposia on Quantitative Biology, **51**, 263 (1986).

[2] C. T. Wittwer and D. J. Garling, "Rapid cycle DNA amplification: Time and temperature optimization," BioTechniques, **10**, 76 (1991).

[3] L. A. Christel, K. Petersen, W. McMillan, and M. A. Northrup, "Rapid, automated nucleic acid probe assays using silicon microstructures for nucleic acid concentration," J. Biomech. Eng., **121**, 22 (1999).

[4] P. Belgrader, W. Benett, D. Hadley, J. Richards, P. Stratton, R. Mariella, and F. Milanovich, "Infectious disease - PCR detection of bacteria in seven minutes," Science, **284**, 449 (1999).

[5] M. Krishnan, V. M. Ugaz, and M. A. Burns, "PCR in a Rayleigh-Benard convection cell," Science, **298**, 793 (2002).

[6] Benett, W. J.; Richards, J. B.; Milanovich, F. P. Convectively Driven PCR Thermal-Cycling. US Patent 6,586,233 B2, July 1, 2003.

[7] Wheeler, E. K.; Benett, W.; Ness, K.; Stratton, P.; Richards, J.; Weisgraber, T. Papavasiliou, A. Laboratory Directed Research and Development FY2001 Annual Report, UCRL-LR-113717-01, 3-8, 2001. http://www-eng.llnl.gov/eng_llnl/01_html/pdfs/ETR_01_PDFs/Vol1_LDRD.pdf.

[8] E. K. Wheeler, W. Benett, P. Stratton, J. Richards, A. Chen, A. Christian, K. D. Ness, J. Ortega, L. G. Li, T. H. Weisgraber, K. Goodson, and F. Milanovich, “Convectively Driven Polymerase Chain Reaction Thermal Cycler,” Anal. Chem., **76**, 4011 (2004).

[9] D. Braun, N. L. Goddard, and A. Libchaber, "Exponential DNA replication by laminar convection," Physical Review Letters, **91**, 158103 (2003).

[10] R. K. Shah and A. L. London, in *Laminar Flow Forced Convection in Ducts*, edited by T. F. Irvine (Academic Press, Inc., New York, 1978), Vol. **1**, Chap. VII, p.213.

[11] B. Gebhart, Y. Jaluria, R. L. Mahajan, and B. Sammakia, *Buoyancy-Induced Flows and Transport* (Hemisphere Publishing Corporation, New York, 1988), Vol. **1**, Chap. 14, p.725.

[12] J. B. Keller, "Periodic oscillations in a model of thermal convection," J. Fluid Mech., **26**, 599 (1966).

[13] P. Welander, "On the oscillatory instability of a differentially heated fluid loop," J. Fluid Mech., **29**, 17 (1967).

[14] R. Greif, Y. Zvirin, and A. Mertol, "The transient and stability behavior of a natural convection loop," J. Heat Transfer, **101**, 684 (1979).

[15] R. Greif, "Natural convection loops," J. Heat Transfer, **110**, 1243 (1988).

[16] C. H. Stern, R. Greif, and J. A. C. Humphrey, "An experimental study of natural convection in a toroidal loop," J. Heat Transfer, **110**, 877 (1988).

[17] S. Kakac, W. Aung, and R. Viskanta, *Natural Convection Fundamentals and Applications* (Hemisphere Publishing Corporation, New York, 1985), Vol. **1**, Chap. Applications, p.1033.

[18] P. S. Damerell and R. J. Schoenhals, "Flow in a toroid; thermosyphon with angular displacement of heated and cooled sections," J. Heat Transfer, **101**, 672 (1979).

[19] S. V. Patankar, *Numerical Heat and Fluid Flow* (Hemisphere Publishing Corporation, New York, 1980).

[20] F. M. White, *Viscous Fluid Flow*, **2**nd edition (McGraw-Hill, Inc., New York, 1991), Vol. **1**, Chap. 3, p.119.

[21] J. Ortega, "A computational study of low-Reynolds number flow in a PCR flow chamber," LLNL internal document, 2002.